ACS APPLIED MATERIALS & INTERFACES

Research Article

www.acsami.org

Coaxial-Electrospun Magnetic Core–Shell Fe@TiSi Nanofibers for the Rapid Purification of Typical Dye Wastewater

Sihui Zhan,*[,†,‡] Dandan Zhu,[†] Guangyuan Ren,[†] Zhiqiang Shen,*[,§] Mingying Qiu,*[,†] Shanshan Yang,[†] Hongbing Yu,[†] and Yi Li[∥]

[†]College of Environmental Science and Engineering, Key Laboratory of Environmental Pollution Process and Environmental Criteria, Nankai University, Tianjin 300071, P. R. China

[‡]Department of Chemistry and Biochemistry, University of Notre Dame, Notre Dame, Indiana 46556, United States

[§]Key Laboratory of Risk Assessment and Control for Environment and Food Safety, Institute of Health and Environmental Medicine, Tianjin 300050, P. R. China

[∥]Department of Chemistry, Tianjin University, Tianjin 300072, P. R. China

ABSTRACT: Magnetic mesoporous γ-Fe_2O_3@$Ti_{0.9}Si_{0.1}O_2$ (abbreviated as Fe@TiSi) core–shell nanofibers were prepared using sol–gel chemistry combined with coaxial-electrospinning technology by adjusting the inner and outer feed ratios. The properties of these novel core–shell nanofibers were characterized by SEM, HRTEM, XRD, FTIR, BET, XPS, and UV–vis spectra. To evaluate the chemical properties of the nanofibers for cleaning typical organic wastewater, methylene blue (MB) was used as a target organic pollutant and was cleaned under irradiation with sunlight and visible light. The Fe@TiSi hierarchical nanofibers composed of a 1:10 feed ratio displayed a mesoporous structure and showed the highest photocatalytic activity for the degradation of MB in water. Furthermore, 86.8% and 71.1% of the MB, which was added at an original concentration of 1 mg/L, was removed after 60 min of irradiation with sunlight and visible light in the presence of Fe@TiSi at a concentration of 0.2 g/L, and 100% of the MB was removed after 75 min. It is very important that the magnetic nanofibers could be recycled rapidly with an outside magnet, and the actual water treatment process was easy to achieve. Moreover, the mechanism of MB degradation by Fe@TiSi core–shell nanofibers was proposed.

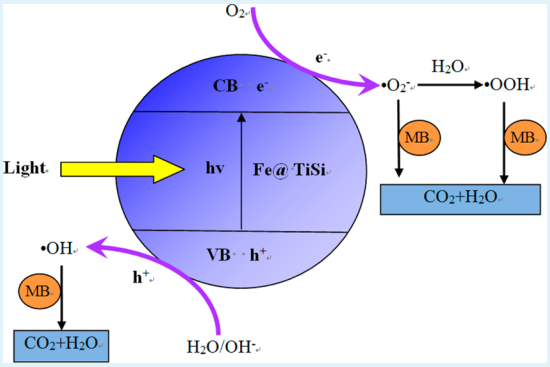

KEYWORDS: *core–shell, magnetic, mesoporous nanofibers, MB, photodegradation*

1. INTRODUCTION

Because of its dark color, high toxicity, and low bioavailability,[1] the cleaning of dyeing wastewater is an urgent scientific problem in the field of environmental protection. Physical–chemical methods and biological methods, such as adsorption,[2,3] biochemical methods,[4,5] and photocatalytic oxidation,[6−9] have been developed for cleaning dyeing wastewater. Among these methods, semiconductor-based photocatalytic reaction has drawn intense interest as a replacement method for water and air purification. Because of its easy operation, low energy consumption, and simple reaction conditions,[10−12] TiO_2 photocatalysis has been extensively studied with regard to its application in environmental remediation processes.

However, there are several drawbacks limiting the use of pure TiO_2 nanoparticles for cleaning dyeing wastewater: (1) low response to visible light, (2) difficult recycling and reuse of TiO_2 particles, (3) secondary pollution, and (4) waste of resources.[11,12] Many studies, including the use of nonmetal element doping,[13−15] noble metal deposition,[16−18] and semiconductors coupling,[19,20] have been conducted to extend the response of TiO_2 to the visible region. In addition, it is necessary to develop much simpler and more convenient immobilization and recycling methods for TiO_2 due to its difficult adhesion on substrate materials (such as glass, zeolites, polymer fibers, and carbon materials), which will result in serious secondary pollution in water environments.[21,22]

One-dimensional nanostructured materials, such as fibers, wires, and tubes, show novel physical and chemical properties that make them promising candidates for applications in environmental processes, energy storage, semiconductors, and sensors.[22] In catalytic processes, pore diffusion resistance is significant for particle-shaped catalysts, which causes many serious problems, such as high pressure drops in industrial applications.[23] Therefore, new forms and morphologies of catalysts, such as nanofibers catalysts, are constructed for a particular use and show very low resistance to diffusion.[24,25] Electrospinning is a popular and simple method for the fabrication of continuous ultrafine fibers with nanometer and

Received: June 29, 2014
Accepted: September 16, 2014
Published: September 16, 2014

submicrometer sizes from polymer solutions or melts.[26] The obtained nanofibers have fibrous mat structures, large surface areas, and sufficient mechanical integrity and are widely applied in many fields.[27] Moreover, coaxial-electrospinning technology makes it easy to obtain many different hierarchical nanostructured materials, such as core/shell fibers, hollow fibers, and tubes, by controlling the flow rate between the inner and outer solutions.[28]

Due to their easy recovery by an outside magnet,[29] magnetic nanomaterials are attracting more and more attention in wastewater treatment.[30] To overcome the difficulty in recycling and reusing TiO_2 particles and secondary pollution, magnetic nanomaterials have been prepared successfully through coaxial-electrospinning technology in the paper. However, the use of magnetic particles is limited due to their easy oxidation/dissolution.[31,32] So, the novel core−shell hierarchical structure has been developed to protect magnetic particles against oxidation because of their advanced properties and multifunctionality.[21]

In this work, we prepared core−shell structured magnetic γ-Fe_2O_3@$Ti_{0.9}Si_{0.1}O_2$ (abbreviated as Fe@TiSi) nanofibers for the first time by coaxial-electrospinning, calcination, and H_2 reduction treatment. The magnetic γ-Fe_2O_3 core can act as a support and magnet, and the mesoporous $Ti_{0.9}Si_{0.1}O_2$ shell can act as a visible-light photocatalyst, which is very important for environmental engineering and wastewater treatment. To our knowledge, the electrospun magenetic core−shell nanofibers have not been reported until now. The formation and properties of the Fe@TiSi nanofiber were assessed through SEM, HR-TEM, XRD, and XPS analyses. By varying the inner and outer feed ratios, several magnetic core−shell nanofibers with different core/shell content ratios were successfully prepared. To verify the photocatalytic properties of these magnetic Fe@TiSi core−shell nanofibers for the treatment of dyeing wastewater, methylene blue (MB) was chosen as a target pollutant under both sunlight and visible light. Moreover, its degradation mechanism was also proposed.

2. EXPERIMENTAL SECTION

2.1. Chemical and Materials. Titanium *n*-butoxide (Ti-$(OC_4H_9^n)_4$, TBOT), tetraethoxysilane ($Si(OC_2H_5)_4$ TEOS), hydrochloric acid (HCl, 36.0%), polyvinylpyrrolidone (PVP, M_w = 1 300 000), ferric chloride hexahydrate ($FeCl_3{\cdot}6H_2O$), pluronic P123 (BASF), ethanol (>99.7%), and methylene blue (MB, $C_{16}H_{18}ClN_3S$) were purchased from Sinopharm Chemical Reagent Corporation and used without further purification.

2.2. Preparation of Core−Shell Nanofibers. The $Ti_{0.9}Si_{0.1}O_2$ spinnable precursor sol was synthesized according to our earlier research results.[33] In a typical process, 2 g of P123 was dissolved into 8 mL of ethanol with stirring to obtain solution A. In addition, 3.56 g of TBOT and 0.218 g of TEOS were added to 4 mL of ethanol to obtain solution B under vigorous stirring, and the Si/Ti molar ratio in this solution was fixed to 10%. Then, 0.6 g of HCl was added to solution B to adjust the pH to the acidic range in order to avoid alkoxide hydrolysis. After complete dissolution, solution A was mixed with solution B to obtain a homogeneous transparent solution, which was then incubated at 55 °C for 10 h to obtain the $Ti_{0.9}Si_{0.1}O_2$ spinnable precursor sol.

Moreover, 2.25 g of $FeCl_3{\cdot}6H_2O$ and 2 g of PVP were dissolved into 6 mL of pure ethanol with vigorous stirring, and the mixture was then incubated at 45 °C for 3 h to obtain the Fe_2O_3 spinnable precursor solution.

After the $Ti_{0.9}Si_{0.1}O_2$ precursor and Fe_2O_3 precursor sol with optimal viscosity were prepared, both were transferred into a coaxial-electrospinning device (Figure 1), which was driven with a microfeed

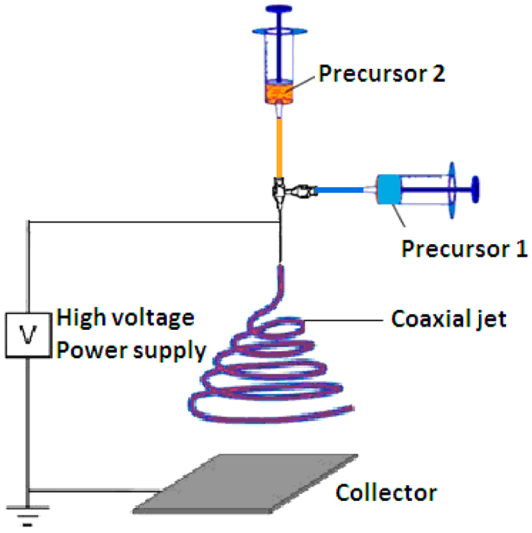

Figure 1. Coaxial-electrospinning apparatus.

pump (Cole-Parmer 74900-05, USA), and a metallic hollow needle was connected to a high-voltage supply (DW-P503-4ACCD, Tianjin, China). A piece of self-made stainless steel board was set under the bottom to collect the electrospun gel fibers at room temperature. In a typical coaxial-electrospinning process, the applied voltage was 15 kV, and the distance between the spinneret and collector was 10 cm. The inner Fe_2O_3 precursor was pressed at a fixed rate of 1 mL/h, and the outer $Ti_{0.9}Si_{0.1}O_2$ precursor was pumped out with an adjustable feed rate (5 mL/h, 10 mL/h, and 15 mL/h). After complete hydrolysis in air for 24 h, the xerogel fibers were obtained. To completely remove the organics, the obtained xerogel fibers were sintered at 130 °C for 4 h, and the temperature was then increased to 400 °C at a heating rate of 0.5 °C·min^{-1} for 4 h. The composite nanofibers were calcined in H_2 atmosphere at 400 °C for 4 h to change the α-Fe_2O_3 core into magnetic γ-Fe_2O_3. After cooling to room temperature naturally, Fe@TiSi (x) core−shell nanofibers with different feed ratios were obtained ("x" represents the Fe_2O_3/$Ti_{0.9}Si_{0.1}O_2$ feed ratio; x = 1:5, 1:10, and 1:15; these core−shell nanofibers are abbreviated as Fe@TiSi(1:5), Fe@TiSi (1:10), and Fe@TiSi (1:15) nanofibers, respectively).

2.3. Characterization. The morphology of the nanofibers was observed through scanning electron microscopy (SEM, TDCLS4800) and high-resolution transmission electron microscopy (HRTEM, Tecnai G2F20). Thermal gravimetric analysis (TGA) was operated under a gas flow of 20 mL·min^{-1} and a heating rate of 10 °C·min^{-1} using a thermal analyzer (PTC-10A). The crystalline structure and microscopic groups of the nanofibers were observed using Fourier transform infrared spectroscopy (FTIR, Biorad FTS6000). The X-ray diffraction (XRD) patterns of the fibers were recorded via an X-ray diffractometer (Rigaku D/Max 2200PC) with a graphite monochromator and Cu Kα radiation (λ = 0.15418 nm) in the range of 10−70° at room temperature, and the voltage and electric current were fixed to 28 kV and 20 mA. The N_2 adsorption−desorption isotherms were recorded via a Quantachrome AutoSorb iQ-MP. The UV−vis absorption spectra of the Fe@TiSi nanofibers were obtained from the dry-pressed disk samples using a UV−vis spectrophotometer (UV-3600). The oxidation state and concentration of the sample surface were observed using X-ray photoelectron spectroscopy (XPS, ESCALAB 250 multitechnique X-ray photoelectron spectrometer (UK)) with a monochromatic AlKα X-ray source ($h\nu$ = 1486.6 eV). All of the XPS spectra were recorded using an aperture slot of 300*700 μm; the survey spectra were recorded with a pass energy of 160 eV, and the high-resolution spectra were recorded with a pass energy of 40 eV. The total organic carbon (TOC) results were recorded via TOC analyzer (TOC-V CSH, Shimadzu, Japan).

2.4. Photocatalytic Degradation of MB. The photocatalytic activities of the Fe@TiSi magnetic core−shell nanofibers with different inner outer feed ratios were determined by cleaning MB under

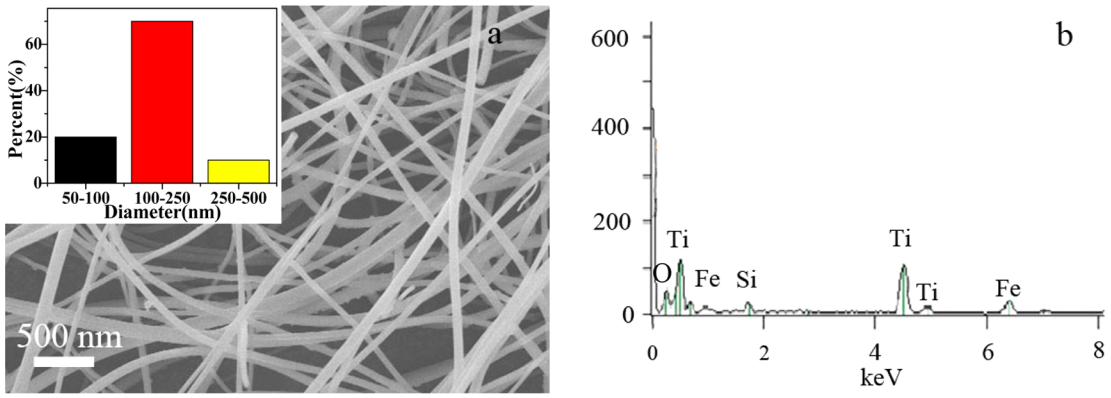

Figure 2. (a) SEM image (the diameter distribution is shown in the inset) and (b) element analysis of typical Fe@TiSi nanofibers with a feed ratio of 1:10.

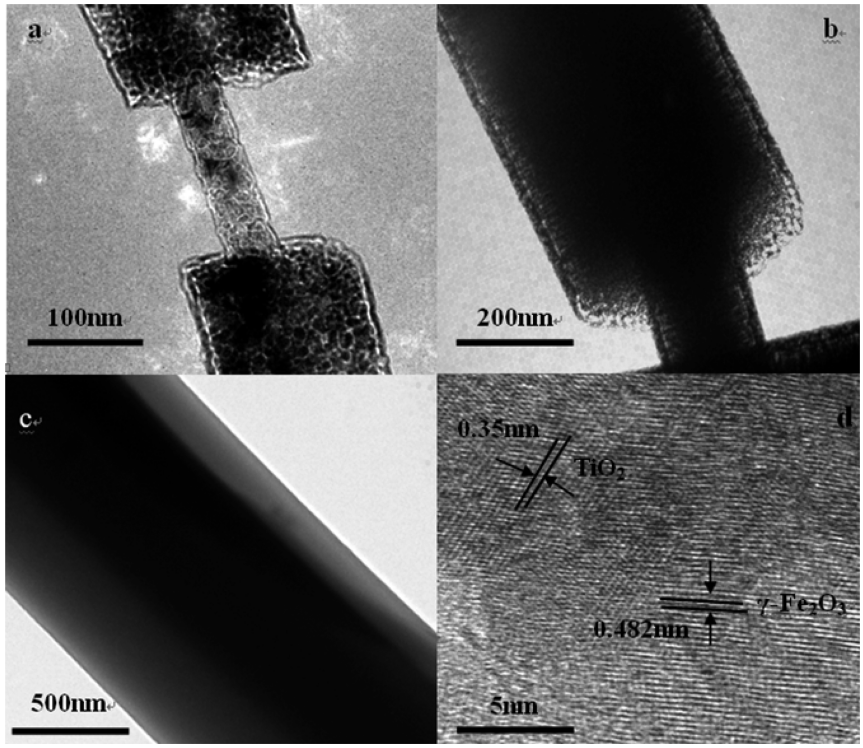

Figure 3. Typical TEM images of Fe@TiSi nanofibers with different inner/outer feed ratios: (a) 1:5, (b) 1:10, and (c) 1:15. (d) HRTEM image of Fe@TiSi (1:10) fibers.

sunlight and visible light. First, 0.02 g of the Fe@TiSi core−shell magnetic nanofibers was added into 100 mL of 1 mg/L MB solution, and the mixture was placed in the dark for 0.5 h with stirring before the photocatalytic reaction to achieve adsorption equilibrium on the surface of the fibrous catalysts. Then, the MB solution was irradiated by a 400 W xenon lamp (Shanghai Yaming Co., China) used as sunlight source, and the visible light source was obtained by adding a UV-filter below xenon lamp. The concentration of MB was detected at intervals of 10 min. For comparison, blank experiments without any catalyst or with $Ti_{0.9}Si_{0.1}O_2$ or pure TiO_2 as the catalyst were also conducted under the same conditions. Using an outside magnetic field, recycled Fe@TiSi nanofibers were subjected to this experiment three times under the same conditions.

The degradation rate of MB in water can be calculated by the following equation, in which C_t is the concentration of MB after several regular intervals of time (t), and $C_{t=0}$ is the initial concentration of MB

$$\text{Degradation rate } \eta(\%) = \frac{C_{t=0} - C_t}{C_{t=0}} \times 100\%$$

3. RESULTS AND DISCUSSION

3.1. Microstructure Investigation. The SEM image and the elemental analysis of typical Fe@TiSi (1:10) nanofibers are shown in Figure 2. Based on their cross sections, it can be observed clearly that the nanofibers exhibited uniform diameters ranging from 50 to 500 nm. From the diameter distribution of Fe@TiSi (1:10) nanofibers, 70% Fe@TiSi (1:10) nanofibers with diameter from 50 to 250 nm can be found. The surface of Fe@TiSi nanofibers is smooth with lengths ranging from 10 to 50 cm. The specific core−shell structure of the Fe@TiSi nanofibers will be further confirmed by the TEM images. Besides, energy dispersive X-ray spectroscopy (EDS) was conducted to analyze the chemical

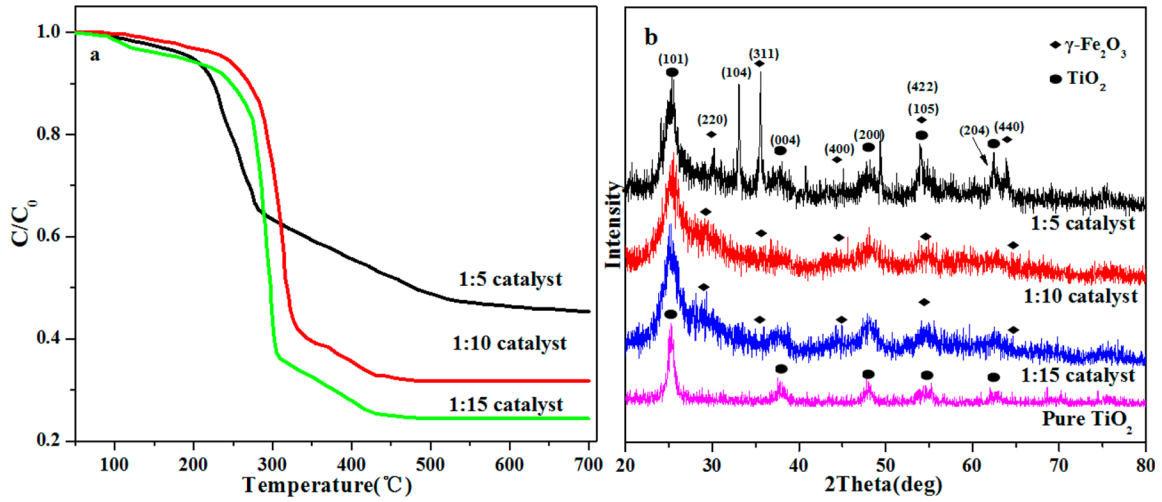

Figure 4. (a) TG and (b) XRD curves of the magnetic Fe@TiSi core–shell nanofibers.

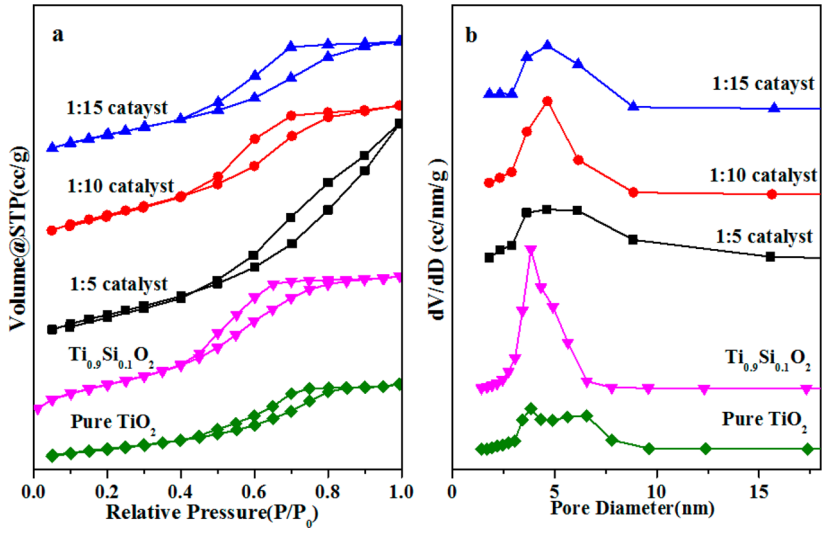

Figure 5. (a) N_2 adsorption–desorption isotherms and (b) pore diameter distribution of magnetic Fe@TiSi core–shell nanofibers and TiSi nanofibers.

composition of Fe@TiSi nanofibers, which obviously proves that Fe@TiSi nanofibers are composed of Fe, Ti, and Si. Based on the elemental analysis of the Fe@TiSi nanofibers (1:10), the mass fractions of Fe, Ti, and Si were found to be 0.81, 12.73, and 7.73, respectively.

To further study the microstructures of the fibers, typical TEM images of the Fe@TiSi (1:5, 1:10, and 1:15) magnetic nanofibers were collected (Figure 3). It can be seen obviously that the Fe@TiSi (1:5, 1:10, and 1:15) magnetic core–shell nanofibers exhibit typical core–shell structures. As shown in Figure 3a, at an inner/outer feed ratio of 1:5, the average core diameter and outer layer are 45 and 50 nm, respectively. As shown in Figure 3b, the γ-Fe_2O_3 core and shell diameter are 170 and 120 nm with an inner/outer feed ratio of 1:10. Moreover, when the inner/outer feed ratio was increased to 1:15, the thickness of the γ-Fe_2O_3 core and outer TiSi layer increased to 625 and 310 nm. As illustrated in the typical HRTEM image of Fe@TiSi (1:10) shown in Figure 3d, there are two obvious lattice fringes that belong to the (101) crystallographic planes of anatase (d_{101} = 0.35 nm)[15] and the (111) crystallographic planes of γ-Fe_2O_3 (d_{111} = 0.482 nm),[34] which is consistent with the hierarchical structure of the composite fiber.

To evaluate the framework stability of the Fe@TiSi magnetic core–shell nanofibers with different inner/outer feed ratios upon heat treatment, it was quantitatively determined by TG analysis under an air atmosphere before calining. According to the TG curves (Figure 4a), all of the volatiles (e.g., ethanol), organic components (P123 and PVP), and Cl^- groups are completely removed at 400 °C in the three samples. The TG curves show three steps and the total weight losses are 54.8% for Fe@TiSi (1:5), 68.1% for Fe@TiSi (1:10), and 53.3% for Fe@TiSi (1:15), respectively. The first minor weight loss before 200 °C is attributed to the removal of physically adsorbed water. The significant weight losses ranging from 200 to 400 °C are attributed to the complete decomposition of ferric chloride, tetrabutyl titanate, TEOS, P123, and PVP. Other minor weight losses are due to further degradation of the organic components.[35] It is obvious that the weight loss is different among three samples, which may be due to the absorbed water, humidity, and temperature.[33,35]

The XRD patterns of the magnetic Fe@TiSi (1:5, 1:10, and 1:15) nanofibers and pure TiO_2 nanofiber are shown in Figure

4b, which shows that Fe@TiSi (1:5, 1:10, and 1:15) nanofibers are composed of titania and γ-Fe_2O_3. The peaks of γ-Fe_2O_3 (JCPDS No. 39−1346) belong to the rhombus structure, whereas the other peaks correspond to anatase TiO_2 (JCPDS No. 21-1272). Based on the XRD pattern of Fe@TiSi (1:5), it can be observed that the five high-intensity peaks in the range $2\theta = 20-80°$ can be indexed as the (220), (311), (400), (422), and (440) diffraction planes for γ-Fe_2O_3 (JCPDS No. 39−1346), and the five crystal peaks can be indexed as the (101), (004), (200), (105), and (204) diffraction planes of anatase TiO_2 (JCPDS No. 21-1272). Meanwhile, the peaks of anatase TiO_2 for Fe@TiSi (1:10) and Fe@TiSi (1:15) magnetic core−shell nanofibers also can be seen. However, the diffraction peaks of γ-Fe_2O_3 observed in the XRD patterns of Fe@TiSi (1:10) and Fe@TiSi (1:15) are weaker than those found in XRD pattern of Fe@TiSi (1:5), which due to that the γ-Fe_2O_3 core was completely coated by the thicker TiSi shell with the increase of TiSi feed rate. In addition, it is found that the relative intensity of TiO_2 peaks of pure TiO_2 nanofibers become decrease compared with the relative intensity of TiO_2 peaks of Fe@TiSi nanofibers, indicating that the TiO_2 crystallite sizes of Fe@TiSi nanofibers are smaller than those of pure TiO_2 nanofibers.[35,36] Based on the Scherrer equation, the average sizes of the TiO_2 found in Fe@TiSi (1:5, 1:10, and 1:15) are 13, 22, and 13 nm, respectively; the average sizes of the γ-Fe_2O_3 found in Fe@TiSi (1:5) is 38 nm.[36] No silica diffraction peak was found because of its low content and amorphous structure.

The N_2 adsorption−desorption isotherms and the pore diameter distribution of the core−shell Fe@TiSi nanofibers (1:5, 1:10, and 1:15) are shown in Figure 5, and the data of the pore size distribution, pore volume, and surface area are listed in Table 1. As shown in Figure 5a, all of the Fe@TiSi core−shell nanofibers with different inner/outer feed ratios, $Ti_{0.9}Si_{0.1}O_2$ nanofibers, and the pure TiO_2 nanofibers show typical IV curves and H1 type hysteresis loops, indicating the presence of uniform mesoporous channels.[6] At a low relative pressure (below 0.5), the isotherm increases slowly. However, at high relative pressure, i.e., between 0.5 and 1.0, the adsorption increases rapidly. Based on the data shown in Figure 5b, it can be observed that the pore size distribution of Fe@TiSi nanofibers (1:5) is from 3.75 to 6.25 nm and the pore size distribution of Fe@TiSi nanofibers (1:10 and 1:15) is centered on 5 nm, which is narrower compared with pure TiO_2 nanofibers with 3−7 nm.

Table 1. Specific Area Distribution, Pore Volume Distribution, and Pore Diameter Distribution of $Ti_{0.9}Si_{0.1}O_2$ and Fe@TiSi Nanofibers with Different Inner/Outer Feed Ratios

materials	specific area (m^2/g)	pore volume (cc/g)	pore diameter (nm)
Fe@TiSi (1:5) fibers	305.530	0.511	4.606
Fe@TiSi (1:10) fibers	308.099	0.344	4.647
Fe@TiSi (1:15) fibers	260.592	0.291	4.650
$Ti_{0.9}Si_{0.1}O_2$ fibers	319.282	0.338	3.836
Pure TiO_2 fibers	100.133	0.189	3.821

As shown in Table 1, the BET surface areas of the Fe@TiSi nanofibers (1:5, 1:10, and 1:15), $Ti_{0.9}Si_{0.1}O_2$ and pure TiO_2 nanofibers are 305.530, 308.099, 260.592, 319.282, and 100.133m^2/g, respectively, and the corresponding pore volumes are 0.511, 0.344, 0.291, 0.338, and 0.189 cm^3/g. As we can see, the surface area, pore volume, and pore diameter are different between Fe@TiSi core−shell nanofibers and $Ti_{0.9}Si_{0.1}O_2$ nanofibers, which is because γ-Fe_2O_3 does not have mesoporous channels, with lower surface area, with the result that the addition of γ-Fe_2O_3 core changed the relative surface area, the pore volume, and the pore diameter of $Ti_{0.9}Si_{0.1}O_2$ nanofibers. The Fe@TiSi nanofibers (1:10) have the largest surface area among the three core−shell nanofibers, indicating that these may exhibit higher photodegradation efficiency compared with Fe@TiSi nanofibers (1:5 and 1:15), which can be confirmed by the following photodegradation results. In addition, the pore size distribution and uniformity of the three core−shell nanofibers are 4.606, 4.647, and 4.650 nm, respectively, demonstrating that the feed ratio has little effect on the pore diameter.

The composition and structure of the nanofibers can also be confirmed by their FTIR spectra (Figure 6). As shown in Figure 6a, the characteristic peaks at approximately 3404 and 1630 cm^{-1} can be assigned to the −OH group and the H−O−H stretching and bending vibrations of the adsorbed water molecules and the Si−OH group of the magnetic Fe@TiSi nanofibers, respectively.[6,7] However, the peaks centered on the 3404 and 1630 cm^{-1} for the sintered nanofibers do not vanish, which may be because H_2O in the air was adsorbed on the fibrous surface, as shown in Figure 6b.[6,37] Moreover, on Figure 6a, the peak at 2970 cm^{-1} originates from the stretching vibration of the C−H band of P123, PVP, and the organic solvent, and the peaks from 1500 to 1375 cm^{-1} can be assigned to the −C−H and −C═C− bands of P123, PVP, and organic solvents.[6,33] However, these peaks disappeared after calcination, as shown in Figure 6b, which demonstrates that P123, PVP, and the organic solvent molecules are removed by sintering. The peaks at 1110 and 1200 cm^{-1} are due to asymmetric Si−O−Si stretching vibrations associated with the motion of oxygen in Si−O−Si antisymmetric stretching.[7,37] The band at 799 cm^{-1} is assigned to Si−O−Si symmetric stretching. The band at approximately 920 cm^{-1} is assigned to the asymmetric Ti−O−Si vibration of TiO_2 and SiO_2 mixed oxides,[7] indicating a local impurity mode of one $-SiO_4$ structural unit banded to Ti^{4+}. According to the FTIR analysis, both Si−O−Si and Si−O−Ti bands are formed. However, no peak for γ-Fe_2O_3 was found, indicating that the γ-Fe_2O_3 core is completely covered by the $Ti_{0.9}Si_{0.1}O_2$ outer layer, as was been verified with the XRD patterns.

The XPS full spectra of Fe@TiSi (1:5, 1:10, and 1:15) are shown in Figure 7. In the wide XPS spectrum (Figure 7a), the three different major peaks can be assigned to Fe 2p, Ti 2p, and Si 2p. Because of the traces of iron content and the outer covering of TiSi composite, the Fe 2p peak of Fe@TiSi (1:10 and 1:15) is not observed.[38] When the inner/outer feed ratio is 1:5, the peaks at 711.21 and 724.9 eV can be assigned to the Fe 2p3/2 and Fe 2p1/2 of γ-Fe_2O_3.

As shown in Figure 7c, the peaks at 458 and 464 eV belong to the Ti 2p3/2 and Ti 2p1/2 of TiO_2. In addition, the peaks are stronger with an increase in the feed ratio, which result in a greater titanium content in the composite fibers. The Si 2p spectrum of the photoelectron peak at 102 eV is shown in Figure 7d. The Si 2p peak became stronger by increasing inner/outer feed ratio.

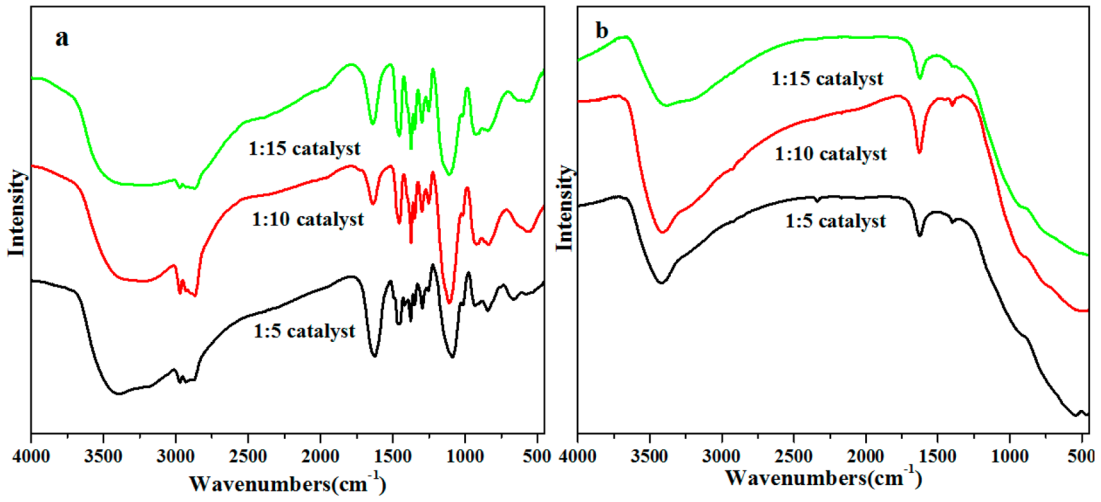

Figure 6. FTIR spectra of the magnetic Fe@TiSi core−shell nanofibers with different inner/outer feed ratios (a) before and (b) after sintering.

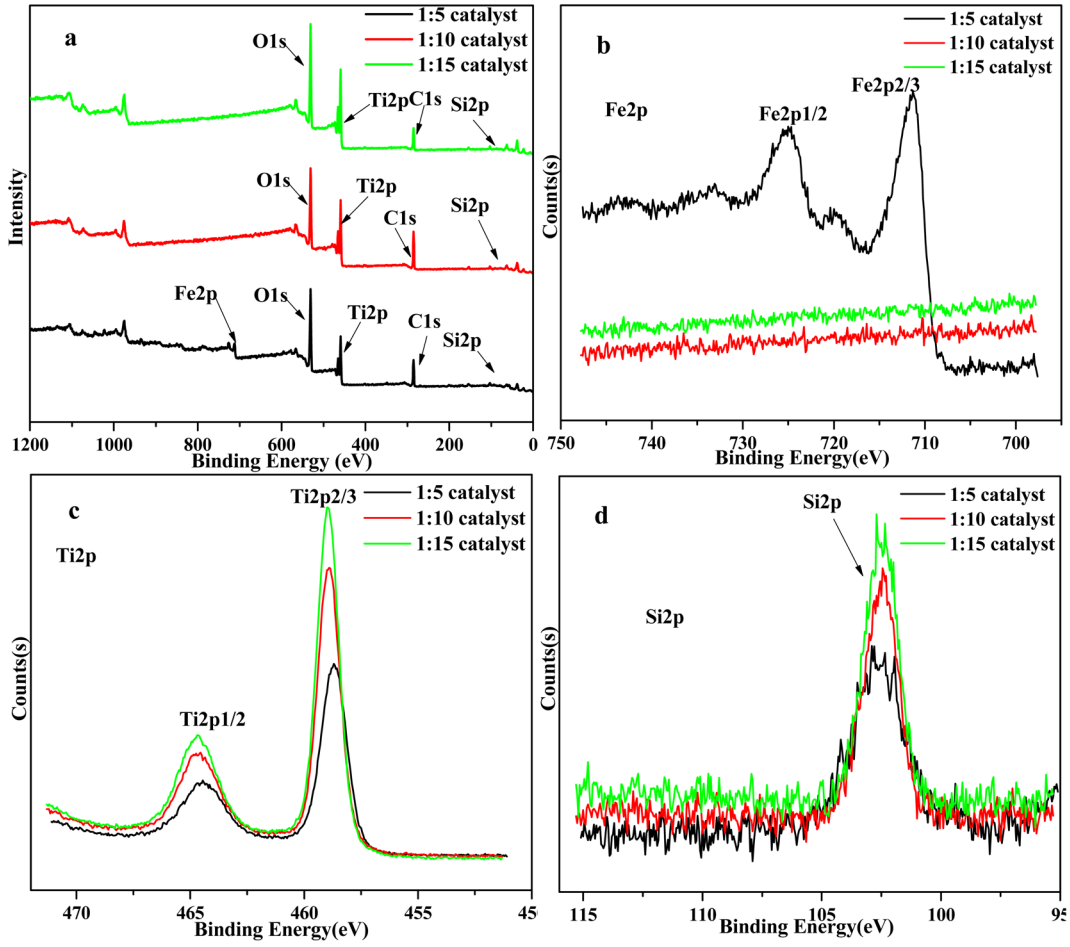

Figure 7. XPS spectrum of the core−shell Fe@TiSi nanofibers with different inner/outer feed ratios: (a) full scale, (b) Fe 2p, (c) Ti 2p, and (d) Si 2p.

3.2. UV−visible Spectrum and Magnetic Properties. The UV−vis spectra of Fe@TiSi (1:5, 1:10, and 1:15) in the wavelength range of 200 to 800 nm are shown in Figure 8a. From 200 to 400 nm, it can be concluded that the Fe@TiSi nanofibers have a broader adsorption area than pure TiO_2 fibers, which indicate that Fe@TiSi nanofibers show better photodegradation efficiency. By the way, the UV−vis absorption data is consistent with the photodegradation results.

The magnetization curves of Fe@TiSi (1:5, 1:10, and 1:15) are shown in Figure 8b. The saturated magnetization (M_s) of Fe@TiSi (1:5) is 1.2 emu·g^{-1}, which is lower than that of bulk γ-Fe_2O_3 because the γ-Fe_2O_3 core is covered by $Ti_{0.9}Si_{0.1}O_2$.[39] The saturated magnetizations (M_s) of Fe@TiSi (1:10 and 1:15) are 0.05 and 0.0002 emu·g^{-1}, respectively. These values are much lower than that of prepared fibers under 1:5 feed ratio, because the γ-Fe_2O_3 core is covered by an outer layer and the γ-

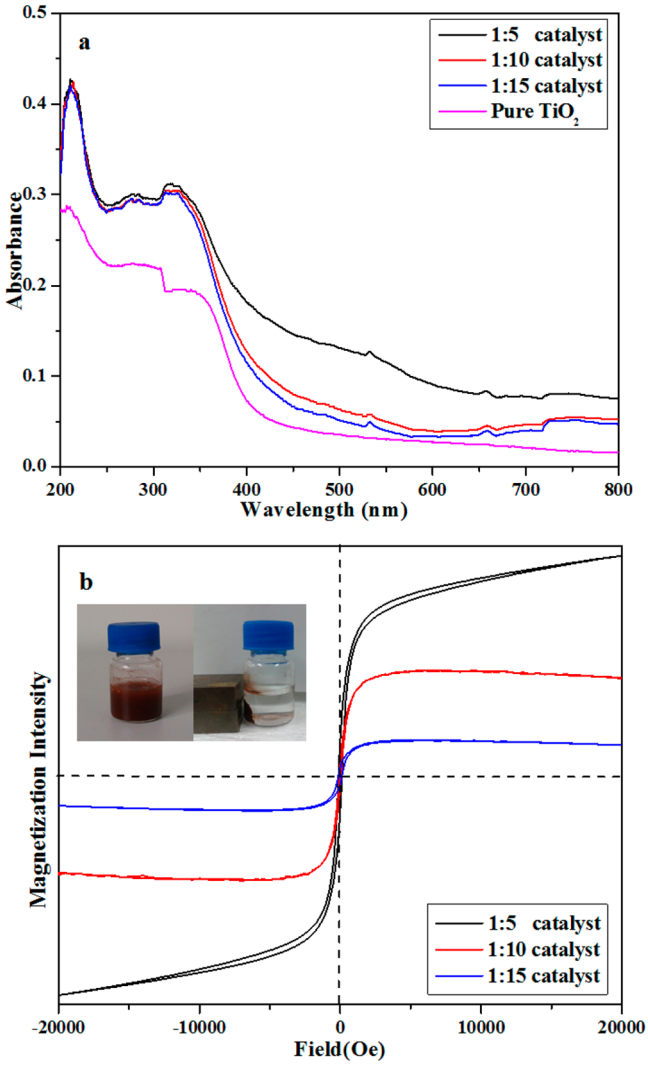

Figure 8. (a) UV–vis spectra and (b) room temperature magnetization curves of Fe@TiSi nanofibers with different inner/outer feed ratios. As shown in the inset in (b), the Fe@TiSi nanofibers can be separated with an outside magnet.

Fe_2O_3 content is relatively reduced. This finding is consistent with the XPS results. As shown in Figure 8b, the magnetic nanofibers can form a dark-brown and stable suspension in water. Using an outer magnet, the magnetic nanofibers can be recycled rapidly, which is important for the recycling of used catalysts.

3.3. Photocatalytic Degradation of MB with Core–Shell Nanofibers. Using Fe@TiSi (1:5, 1:10, and 1:15) as catalysts, their efficiencies for the photodegradation of MB in water under both sunlight and visible light were tested, as shown in Figure 9. As illustrated in Figure 9a, only 5.5% of the MB can be cleaned in the absence of any catalyst under simulated sunlight, indicating that MB is stable and can remain in the natural environment for a long time in the absence of any control measures. From Figure 9a, the photodegradation efficiency of $Ti_{0.9}Si_{0.1}O_2$ with 90% removal efficiency is higher than pure TiO_2 with 62.9% removal efficiency, which indicates that the photocatalytic activity of pure TiO_2 has been enhanced by doping Si. This is because Si doped can effectively inhibit the transfer of photogenerated electrons and holes from TiO_2 into the lower-lying conduction band to enhance the photocatalytic

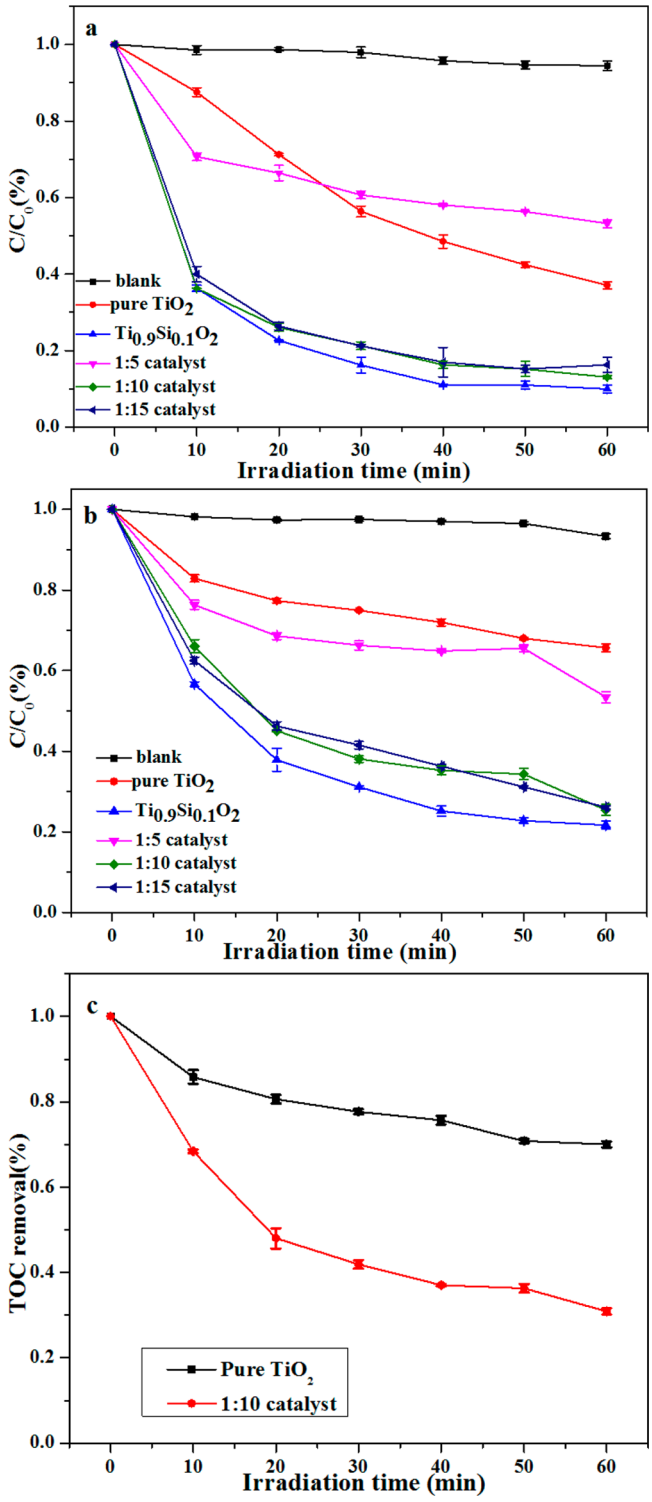

Figure 9. Photodegradation efficiency of MB with Fe@TiSi core–shell nanofibers under (a) sunlight and (b) visible light. (c) TOC removal efficiency of MB under visible light.

activity of TiO_2.[7,36,40] However, the efficiency of the degradation of MB with Fe@TiSi (1:5) is only 46.8%, which is lower than that of pure TiO_2 and other catalysts because the γ-Fe_2O_3 content of Fe@TiSi (1:5) is higher than that of Fe@TiSi (1:10 and 1:15) and $Ti_{0.9}Si_{0.1}O_2$. It should be noted that γ-Fe_2O_3 has no photocatalytic activity. Thus, the degradation efficiencies of Fe@TiSi (1:5, 1:10, and 1:15) are lower than

dx.doi.org/10.1021/am505751z | ACS Appl. Mater. Interfaces 2014, 6, 16841–16850

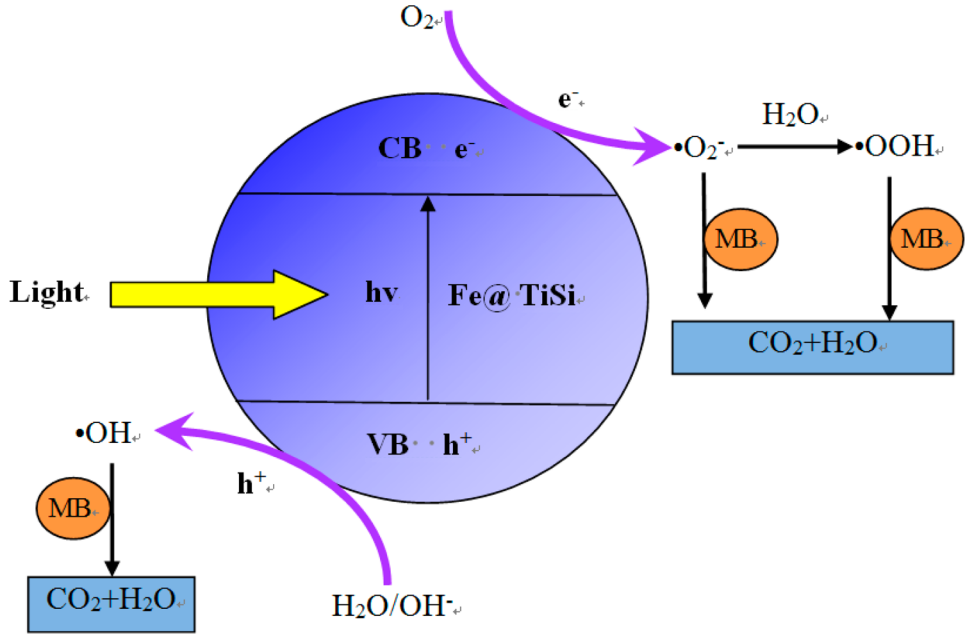

Figure 10. Mechanism for the photocatalytic degradation of MB on the Fe@TiSi core–shell nanofibers.

that of $Ti_{0.9}Si_{0.1}O_2$. In the paper, Fe@TiSi (1:10) and Fe@TiSi (1:15) removed 86.8% and 83.7% of the MB under the same conditions after 60 min, respectively. The degradation efficiency of Fe@TiSi (1:10 and 1:15) is much higher than pure TiO_2, which also is due to doping Si. The doping Si can extend the visible absorption, depress hole–electron recombination, and narrow the band gap of TiO_2, as was confirmed with the UV–vis spectra of the Fe@TiSi nanofibers (Figure 7a). However, additional γ-Fe_2O_3 core can make fibrous catalysts be more easily recycled from water using outside magnets. As shown through repeated experiments using magnetic fibers that were recycled for more than three times, no change in the degradation rate of MB in water was observed after recycling.

The efficiencies of the fibers for the degradation of MB under visible light are shown in Figure 9b. The variation features and trends are similar to those found under solar light (Figure 9a). Under excitation with visible light, the degradation efficiencies of Fe@TiSi (1:5, 1:10, and 1:15), pure TiO_2, and $Ti_{0.9}Si_{0.1}O_2$ are 46.6%, 71.1%, 73.7%, 35%, and 78.7%, respectively, which are lower than those obtained under solar light due to the reduced total lighting energy. Similarly, the efficiencies of Fe@TiSi (1:10 and 1:15) for the degradation of MB are higher than that of pure TiO_2 due to the coupling effect of SiO_2 and TiO_2.

The TOC removal efficiency of MB is as shown in Figure 9c. It can be seen that the TOC removal efficiency becomes higher and higher with the longer irradiation time and the degradation trend is similar to the photodegradation efficiency, which indicates that the MB has been photodegraded to CO_2 and H_2O.

3.4. Photodegradation Mechanism. The possible mechanism of MB photocatalysis on the Fe@TiSi core–shell nanofibers is proposed in Figure 10. First, water, O_2, and MB are adsorbed on the surface of the Fe@TiSi core–shell nanofibers, followed by the formation of hole–electron pairs on the surface of Fe@TiSi nanofibers which need enough light energy to overcome the band gap energy (E_g) between valence band (VB) and conduction band (CB). When the light irradiation with greater energy hit its surface and the light energy exceeds the band energy, the electrons excited from the surface of the Fe@TiSi nanofibers will transfer from the valence band into the conduction band. Then, the hole (h^+) with high activity leaving the valence band may react with H_2O/OH^-; the hydroxyl radicals formed also have strong oxidizing activity.[9,14]

$$h^+ + H_2O \rightarrow \bullet OH + H^+ \quad (1)$$

$$h^+ + OH^- \rightarrow \bullet OH \quad (2)$$

e^- leaved in conduction band may react with O_2 absorbed on the surface of the Fe@TiSi nanofibers.

$$O_2 + e^- \rightarrow \bullet O^{2-} \quad (3)$$

$$\bullet O^{2-} + 2H_2O \rightarrow \bullet OOH + 2OH^- \quad (4)$$

$$\bullet OOH + H_2O + e - \rightarrow H_2O_2 + OH^- \quad (5)$$

$$H_2O_2 + e^- \rightarrow \bullet OH + OH^- \quad (6)$$

$$H_2O_2 + h\nu \rightarrow 2 \bullet OH \quad (7)$$

In addition, these •OH, $\bullet O^{2-}$, and •OOH further react with MB to generate water and CO_2.

The superior photocatalytic activity of the Fe@TiSi core–shell nanofibers is mainly due to the following. First, doping Si can effectively inhibit the combination of photogenerated electron–hole pairs, generate a greater number of electrons and holes, and accelerate the process of the photocatalytic reaction to enhance the photocatalytic activity of TiO_2.[7,40,41] Second, the high surface area, small particle size, and anatase crystal are beneficial to increasing the degradation efficiency.[7,36] In addition, the Fe@TiSi nanofibers have a broader adsorption area than pure TiO_2 fibers, which is beneficial to photodegradation efficiency, as was confirmed by the UV–vis spectra of the Fe@TiSi nanofibers.[40]

4. CONCLUSIONS

In this manuscript, magnetic Fe@TiSi core–shell nanofibers were prepared successfully by sol–gel chemistry combined with

coaxial-electrospinning and were used to clean dyeing wastewaters. Under both solar light and visible light, the efficiencies of the magnetic Fe@TiSi core−shell nanofibers for the degradation of MB were higher than that of pure TiO_2. Magnetic Fe@TiSi nanofibers with an inner/outer feed ratio of 1:10 exhibited the highest photodegradation efficiency of MB in water. The core−shell structured magnetic Fe@TiSi nanofibers exhibited efficient photocatalytic activities for the removal of MB from wastewater and other attractive features: (1) high efficiency, (2) rapid response to visible light, (3) easy recycling, and (4) no pollution and zero energy consumption for reuse using an outer magnet.

AUTHOR INFORMATION

Corresponding Authors

*E-mail: sihuizhan@nankai.edu.cn. Tel/Fax: +86-22-23502756.
*E-mail: szq922990@126.com.
*E-mail: jkcs66902@163.com.

Notes

The authors declare no competing financial interest.

ACKNOWLEDGMENTS

The authors gratefully acknowledge the financial support provided by the National Natural Science Foundation of China (21377061), the Asia Research Center in Nankai University (AS1326), the Natural Science Foundation of Tianjin (12JCQNJC05800), and the Key Technologies R&D Program of Tianjin (13ZCZDSF00300) and the assistance provided by Dr. Raymond Seekell (University of Notre Dame) in the manuscript preparation and discussion.

REFERENCES

(1) Wu, Q. H.; Cheng, F.; Chun, W.; Zhi, W. A Facile One-Pot Solvothermal Method to Produce Superparamagnetic Graphene−Fe_3O_4 Nanocomposite and Its Application in the Removal of Dye from Aqueous Solution. *Colloids Surf., B* **2013**, *101*, 210−214.
(2) Ouyang, X. W.; Li, W.; Xie, S. L.; Zhai, T.; Yu, M. H.; Gan, J. Y.; Lu, X. H. Hierarchical CeO_2 Nanospheres as Highly-Efficient Adsorbents for Dye Removal. *New J. Chem.* **2013**, *37*, 585−588.
(3) Shuang, C. D.; Li, P. H.; Li, A. M.; Zhou, Q. M.; Zhang, C.; Zhou, Y. Quaternized Magnetic Microspheres for the Efficient Removal of Reactive Dyes. *Water Res.* **2012**, *46*, 4417−4426.
(4) Moscofian, A.; Pires, C.; Vieira, A. P.; Airoldi, C. Organo-functionalized Magnesium Phyllosilicates as Mono- or Bifunctitonal Entities for Industrial Dyes Removal. *RSC Adv.* **2012**, *2*, 3502−3511.
(5) Shen, C. S.; Wen, Y. Z.; Kang, X. D.; Liu, W. H_2O_2-Induced Surface Modification: A Facile, Effective and Environmentally Friendly Pretreatment of Chitosan for Dyes Removal. *Chem. Eng. J.* **2011**, *166*, 474−482.
(6) Li, X. C.; V. John, T. J.; Zhan, J.; He, G. H.; He, J. B.; Spinu, L. The Synthesis of Mesoporous $TiO_2/SiO_2/Fe_2O_3$ Hybrid Particles Containing Micelle-Induced Macropores Through an Aerosol Based Process. *Langmuir* **2011**, *27*, 6252−6259.
(7) Yu, X. X.; Liu, S. W.; Yu, J. G. Superparamagnetic γ-Fe_2O_3@SiO_2@TiO_2 Composite Microspheres with Superior Photocatalytic Properties. *Appl. Catal., B* **2011**, *104*, 12−20.
(8) Tian, S. H.; Zhang, J. L.; Chen, J.; Kong, L. J.; Lu, J.; Ding, F. C.; Xiong, Y. $Fe_2(MoO_4)_3$ as an Effective Photo-Fenton-Like Catalyst for the Degradation Of Anionic and Cationic Dyes In A Wide Ph Range. *Ind. Eng. Chem. Res.* **2013**, *37*, 13333−13341.
(9) Hussain, M.; Bensaid, S.; Geobaldo, F.; Saracco, G.; Russo, N. Photocatalytic Degradation Of Ethylene Emitted By Fruits with TiO_2 Nanoparticles. *Ind. Eng. Chem. Res.* **2011**, *50*, 2536−2543.
(10) Westrich, T. A.; Dahlberg, K. A.; Kaviany, M.; Schwank, J. W. High-Temperature Photocatalytic Ethylene Oxidation over TiO_2. *J. Phys. Chem. C* **2011**, *115*, 16537−16543.
(11) Morales-Torres, S.; Pastrana-Martínez, L. M.; Figueiredo, J. L.; Faria, J. L.; Silva, A. Design of Graphene-Based TiO_2 Photocatalysts-a Review. *Environ. Sci. Pollut. Res.* **2012**, *19*, 3676−3687.
(12) He, J. F.; Liu, Q. H.; Sun, Z. H.; Yan, W. S.; Zhang, G. B.; Qi, Z. M.; Xu, P. S.; Wu, Z. Y.; Wei, S. Q. High Photocatalytic Activity of Rutile TiO_2 Induced by Iodine Doping. *J. Phys. Chem. C* **2010**, *114*, 6035−6038.
(13) Wu, X. Y.; Yin, S.; Dong, Q.; Guo, C. S.; Kimura, T.; Matsushita, J.; Sato, T. Photocatalytic Properties of Nd and C Codoped TiO_2 with the Whole Range of Visible Light Absorption. *J. Phys. Chem. C* **2013**, *117*, 8345−8352.
(14) He, Z. L.; Que, W. X.; Chen, J.; Yin, X. T.; He, Y. C.; Ren, J. B. Photocatalytic Degradation of Methyl Orange over Nitrogen-Fluorine Codoped TiO_2 Nanobelts Prepared by Solvothermal Synthesis. *ACS Appl. Mater. Interfaces* **2012**, *4*, 6816−6826.
(15) Nasir, M.; Xi, Z. H.; Xing, M. Y.; Zhang, J. L.; Chen, F.; Tian, B. Z.; Bagwasi, S. Study of Synergistic Effect of Ce- and S-codoping on the Enhancement of Visible-Light Photocatalytic Activity of TiO_2. *J. Phys. Chem. C* **2013**, *117*, 9520−9528.
(16) Dozzi, M. V.; Saccomanni, A.; Selli, E. Cr(VI) Photocatalytic Reduction: Effects of Simultaneous Organics Oxidation and of Gold Nanoparticles Photodeposition on TiO_2. *J. Hazard. Mater.* **2012**, *211−212*, 188−195.
(17) Liu, C.; Yang, D.; Jiao, Y.; Tian, Y.; Wang, Y. G.; Jiang, Z. Y. Biomimetic Synthesis of TiO_2-SiO_2-Ag Nanocomposites with Enhanced Visible-Light Photocatalytic Activity. *ACS Appl. Mater. Interfaces* **2013**, *5*, 3824−3832.
(18) Nishikawa, M.; Mitani, Y.; Nosaka, Y. Photocatalytic Reaction Mechanism of Fe(III)-Grafted TiO_2 Studied by Means of ESR Spectroscopy and Chemiluminescence Photometry. *J. Phys. Chem. C* **2012**, *116*, 14900−14907.
(19) Labiadha, H.; Chaabanea, T. B.; Balanb, L.; Becheikc, N.; Corbelc, S.; Medjahdid, G.; Schneide, R. Preparation of Cu-doped ZnS QDs/TiO_2 Nanocomposites with High Photocatalytic Activity. *Appl. Catal., B* **2014**, *144*, 29−35.
(20) Luo, X. B.; Deng, F.; Min, L. J.; Luo, S. L.; Guo, B.; Zeng, G. S.; Au, C. Facile One-Step Synthesis of Inorganic-Framework Molecularly Imprinted TiO_2/WO_3 Nanocomposite and Its Molecular Recognitive Photocatalytic Degradation of Target Contaminant. *Environ. Sci. Technol.* **2013**, *47*, 7404−7412.
(21) Chen, Y. H.; Li, W. S.; Liu, C. Y.; Wang, C. Y.; Chang, Y. C.; Chen, L. Core-Shell-Structured Carbon Nanofiber-Titanate Nanotubes with Enhanced Photocatalytic Activity. *Appl. Catal., B* **2014**, *148−149*, 170−176.
(22) Di, J. C.; Zhao, Y.; Yu, J. H. Fabrication of Molecular Sieve Fibers by Electrospinning. *J. Mater. Chem.* **2011**, *21*, 8511−8520.
(23) Wen, Q.; Di, J. C.; Zhao, Y.; Wang, Y.; Jiang, L.; Yu, J. H. Flexible Inorganic Nanofibrous Membranes with Hierarchical Porosity for Efficient Water Purification. *Chem. Sci.* **2013**, *4*, 4378−4382.
(24) Fu, Y.; Liu, L.; Zhang, L. Q.; Wang, W. C. Highly Conductive One-Dimensional Nanofibers: Silvered Electrospun Silica Nanofibers via Poly(dopamine) Functionalization. *ACS Appl. Mater. Interfaces* **2014**, *6*, 5105−5112.
(25) Yavuz, C. T.; Mayo, J. T.; Yu, W. W.; Prakash, A.; Falkner, J. C.; Yean, S.; Cong, L. L.; Shipley, H. J.; Kan, A.; Tomson, M.; Natelson, D.; Colvin, V. L. Low-Field Magnetic Separation of Monodisperse Fe_3O_4 Nanocrystals. *Science* **2006**, *314*, 964−967.
(26) Zhao, Y.; Sun, L.; Xi, M.; Feng, Quan.; Jiang, C. Y.; Fong, H. Electrospun TiO_2 Nanofelt Surface-Decorated with Ag Nanoparticles as Sensitive and UV-Cleanable Substrate for Surface Enhanced Raman Scattering. *ACS Appl. Mater. Interfaces* **2014**, *6*, 5759−5767.
(27) Chen, H. Y.; Di, J. C.; Wang, N.; Dong, H.; Wu, J.; Zhao, Y.; Yu, J. H.; Lei Jiang, L. Fabrication of Hierarchically Porous Inorganic Nanofibers by a General Microemulsion Electrospinning Approach. *Small* **2011**, *7*, 1779−1783.

(28) Bedford, N. M.; Steckl, A. J. Photocatalytic Self-Cleaning Textile Fibers by Coaxial Electrospinning. *ACS Appl. Mater. Interfaces* **2010**, *2*, 2448−2455.
(29) Wang, D. L.; Xin, H. L.; Hovden, R.; Wang, H. S.; Yu, Y. C.; Muller, D. A.; DiSalvo, F. J.; Abruña, H. D. Structurally Ordered Intermetallic Platinum−Cobalt Core−Shell Nanoparticles with Enhanced Activity and Stability As Oxygen Reduction Electrocatalysts. *Nat. Mater.* **2013**, *12*, 81−87.
(30) Qiang, Z. M.; Bao, X. L.; Ben, W. W. MCM-48 Modified Magnetic Mesoporous Nanocomposite as an Attractive Adsorbent for the Removal of Sulfamethazine from Water. *Water Res.* **2012**, *47*, 4107−4114.
(31) Zhu, J. H.; Wei, S. Y.; Gu, H. B.; Rapole, S. B.; Wang, Q.; Luo, Z. P.; Haldolaarachchige, N.; Young, D. P.; Guo, Z. H. One-Pot Synthesis of Magnetic Graphene Nanocomposites Decorated with Core@Double-Shell Nanoparticles for Fast Chromium Removal. *Environ. Sci. Technol.* **2012**, *46*, 977−985.
(32) Pinheiro, J. P.; Moura, L.; Fokkink, R.; Farinha, J. Preparation and Characterization of Low Dispersity Anionic Multiresponsive Core-Shell Polymer Nanoparticles. *Langmuir* **2012**, *28*, 5802−5809.
(33) Zhan, S. H.; Yang, Y.; Gao, X. C.; Yu, H. B.; Yang, S. S.; Zhu, D. D.; Li, Y. Rapid Degradation of Toxic Toluene Using Novel Mesoporous SiO_2 Doped TiO_2 Nanofibers. *Catal. Today* **2014**, *225*, 10−17.
(34) Sun, G. B.; Dong, B. X.; Cao, M. H.; Wei, B. Q.; Hu, C. W. Hierarchical Dendrite-Like Magnetic Materials of Fe_3O_4, γ-Fe_2O_3, and Fe with High Performance of Microwave Absorption. *Chem. Mater.* **2011**, *23*, 1587−1593.
(35) Patra, A. K.; Dutta, A.; Bhaumik, A. Highly Ordered Mesoporous TiO_2-Fe_2O_3 Mixed Oxide Synthesized by Sol-Gel Pathway: an Efficient and Reusable Heterogeneous Catalyst for Dehalogenation Reaction. *ACS Appl. Mater. Interfaces* **2012**, *4*, 5022−5028.
(36) Wang, C. X.; Yin, L. W.; Zhang, L. Y.; Kang, L.; Wang, X. F.; Gao, R. Magnetic (γ-Fe_2O_3@SiO_2) @TiO_2 Functional Hybrid Nanoparticles with Actived Photocatalytic Ability. *J. Phys. Chem. C* **2009**, *113*, 4008−4011.
(37) Yu, Y.; Zhang, M. Z.; Chen, J.; Zhao, Y. D. Homogeneous Synthesis of SiO_2@TiO_2 Nanocomposites with Controllable Shell Thickness and Their Enhanced Photocatalytic Activity. *Dalton Trans.* **2013**, *42*, 885−889.
(38) Yang, S. J.; Liu, C. X.; Chang, H. Z.; Ma, L.; Qu, Z.; Yan, N. Q.; Wang, C. Z.; Li, J. H. Improvement of the activity of γ−Fe_2O_3 for the Selective Catalytic Reduction of NO with NH_3 at High Temperatures: NO Reduction Versus NH_3 Oxidization. *Ind. Eng. Chem. Res.* **2013**, *52*, 5601−5610.
(39) Lu, J.; Jiao, X. L.; Chen, D. R.; Li, W. Solvothermal Synthesis and Characterization of Fe_3O_4 and γ-Fe_2O_3 Nanoplates. *J. Phys. Chem. C* **2009**, *113*, 4012−4017.
(40) Daghrir, R.; Drogui, P.; Robert, D. Modified TiO_2 for Environmental Photocatalytic Applications: a Review. *Ind. Eng. Chem. Res.* **2013**, *52*, 3581−3599.
(41) Pinho, L.; Hernández-Garrido, J. C.; Mosquera, J. 2D and 3D Characterization of a Surfactant-Synthesized TiO_2-SiO_2 Mesoporous Photocatalyst Obtained at Ambient Temperature. *Phys. Chem. Chem. Phys.* **2013**, *15*, 2800−2808.